

# X-ray measurement of electron and magnetic-field energy densities in the west lobe of the giant radio galaxy 3C 236

Naoki ISOBE<sup>1,\*</sup> and Shoko KOYAMA<sup>2</sup>

<sup>1</sup>Institute of Space and Astronautical Science (ISAS), Japan Aerospace Exploration Agency (JAXA)  
3-1-1 Yoshinodai, Chuo-ku, Sagami-hara, Kanagawa 252-5210, Japan

<sup>2</sup>Max-Planck-Institut für Radioastronomie, Auf dem Hügel 69, 53121 Bonn, Germany

\*E-mail: [n-isobe@ir.isas.jaxa.jp](mailto:n-isobe@ir.isas.jaxa.jp)

Received 2014 December 17; Accepted 2015 May 7

## Abstract

X-ray emission associated with the west lobe of the giant radio galaxy 3C 236 was investigated with the Suzaku observatory to evaluate the energetics in the lobe. After removing contamination from point-like X-ray sources detected with Chandra and subtracting the X-ray and non-X-ray backgrounds, the Suzaku spectrum from the lobe was reproduced by a power-law model with a photon index of  $\Gamma = 2.23^{+0.44+0.14}_{-0.38-0.12}$ , where the first and second errors represent the statistical and systematic ones, respectively. Within the errors, the X-ray index was consistent with the radio synchrotron one,  $\Gamma_R = 1.74 \pm 0.07$ , estimated in the 326–2695 MHz range. This agreement supports that the X-ray emission is attributed to the inverse-Compton radiation from the synchrotron electrons filling the lobe, where the cosmic microwave background photons are up-scattered. This result made 3C 236 the largest radio galaxy of which the lobe has ever been probed through the inverse-Compton X-ray photons. When the photon index was fixed at  $\Gamma_R$ , the X-ray flux density at 1 keV was measured as  $S_X = 12.3 \pm 2.0 \pm 1.9$  nJy. A comparison of the X-ray flux to the radio one ( $S_R = 1.11 \pm 0.02$  Jy at 608.5 MHz) yields the energy densities of the electrons and magnetic field in the west lobe as  $u_e = 3.9^{+0.6+1.0}_{-0.7-0.9} \times 10^{-14}$  erg cm<sup>-3</sup> and  $u_m = 0.92^{+0.21+0.52}_{-0.15-0.35} \times 10^{-14}$  erg cm<sup>-3</sup>, respectively, indicating a mild electron dominance of  $u_e/u_m = 4.2^{+1.6+4.1}_{-1.3-2.3}$ . The latter corresponds to the magnetic field strength of  $B = 0.48^{+0.05+0.12}_{-0.04-0.10}$   $\mu$ G. These are typical among the lobes of giant radio galaxies. A summary of the  $u_e$ -size relation for the inverse-Compton-detected radio galaxies implies that the west lobe of 3C 236 is still actively energized by its jet.

**Key words:** galaxies: individual (3C 236)—galaxies: jets—magnetic fields—radiation mechanisms: non-thermal—X-rays: galaxies

## 1 Introduction

Radio sources with a total projected size of  $D \gtrsim 1$  Mpc are categorized as giant radio galaxies. They constitute one of the largest classes of astrophysical objects in the Universe. With a typical spectral age  $T_{\text{age}}$  that is higher

than a few 10 Myr (Schoenmakers et al. 2000), they are recognized as relatively old systems. Therefore, the giant radio galaxies are utilized to investigate the activity of jets and associated lobes in evolved radio sources, which is yet to be explored.

**Table 1.** Log of observations.

Observatory	ObsID	Date	(RA, Dec)*	GTI (ks)	Target
Suzaku	707005010	2012 May 6–8	(151°3326, +35°0063)	78.0	West Lobe
Suzaku	707006010	2012 May 8–9	(151°1525, +34°7488)	42.4	XRB
Chandra	10246	2012 March 10	—	29.4	West Lobe

\*The sky coordinates at the XIS nominal position.

Lobes of radio galaxies accumulate an enormous amount of relativistic plasma, comprising electrons, and magnetic field (and possibly heavy particles including protons, although the present paper does not deal with them). The plasma energy in the lobes is sourced from the bulk kinetic energy of the jets through their terminal hot spots. This makes the lobes one of the most valuable probes into the past jet activity. It is possible to estimate roughly the plasma energy in the lobes from their synchrotron radio radiation. However, the radio information alone is not useful for disentangling the electron and magnetic field energies, and thus the minimum energy condition (Miley 1980) was widely assumed, without any concrete physical justification.

More valuable information for the study of the energetics should be provided by inverse Compton (IC) X-ray emission from the synchrotron-emitting electrons in the lobes, where the cosmic microwave background (CMB) photons are boosted up (Harris & Grindlay 1979). The IC X-ray spectrum, in comparison with the synchrotron radio one, enables an independent estimate of the electron and magnetic energies. In the last two decades since its discovery from the lobes of Fornax A (Feigelson et al. 1995; Kaneda et al. 1995), the IC X-ray radiation has been a standard tool to diagnose the lobe energetics (e.g., Tashiro et al. 1998, 2009; Isobe et al. 2002, 2005, 2006; Croston et al. 2005; Migliori et al. 2007; Takeuchi et al. 2012; Stawarz et al. 2013). The technique was strengthened by the IC  $\gamma$ -ray detection with the Fermi observatory from the outer lobes of Centaurus A (Abdo et al. 2010). As a result, the electron energy is found to surpass the magnetic one in the lobes, typically by a factor of 1–100.

Until recently, IC X-ray examination of lobes of giant radio galaxies has been hampered, mainly by their faintness. For diffuse X-ray sources with a low surface brightness, the X-ray Imaging Spectrometer (XIS: Koyama et al. 2007) onboard the Suzaku observatory (Mitsuda et al. 2007) presents a great advantage, owing to its moderate field of view (a  $\sim 18'$  square) and to its rather low and stable instrumental background (Tawa et al. 2008). In fact, a systematic study with the XIS has just been conducted for the lobes of several giant radio galaxies (Isobe et al. 2009, 2011a, 2011b). This research arrived at a significant detection of IC X-ray photons from these lobes, and pioneeringly hinted that the current jet activities are significantly decreased in the giant radio galaxies, compared with those

with a moderate size (e.g.,  $D \lesssim 500$  kpc). This motivates us to enlarge urgently the sample of IC-detected giant radio galaxies.

The giant radio galaxy 3C236 is located at the redshift  $z = 0.1005 \pm 0.0005$  (Hill et al. 1996). Assuming the cosmology with  $H_0 = 71 \text{ km s}^{-1} \text{ Mpc}^{-1}$ ,  $\Omega_m = 0.27$ , and  $\Omega_\lambda = 0.73$ , the redshift gives an angle-to-size conversion ratio of  $109.8 \text{ kpc}/1'$ . It is optically classified as a low-excitation radio galaxy, with weak emission lines (Laing et al. 1983). With a classical Fanaroff–Riley II radio morphology (Laing et al. 1983), the radio source has an angular extent of  $\sim 40'$  (Willis et al. 1974; Strom & Willis 1980), which corresponds to a projected linear size of  $D \sim 4.4 \text{ Mpc}$ . Therefore, this had been known as the largest radio source in the whole sky, until the giant radio galaxy J1420–0545 with a size of  $D \sim 4.7 \text{ Mpc}$  was discovered (Machalski et al. 2008). The age of the source is estimated as  $T_{\text{age}} = 98 \pm 3 \text{ Myr}$  by the synchrotron aging technique (Schoenmakers et al. 2000), indicating that it is really an elderly radio galaxy. These make 3C236 an ideal target for the IC X-ray study with Suzaku. Indeed, a faint X-ray emission associated with its west lobe has been concretely detected in the Suzaku observation, as is reported in the present paper.

## 2 Observation and data reduction

### 2.1 Suzaku observation

The log of the Suzaku observations for the giant radio galaxy 3C236 is given in table 1. We focused on the west lobe, since radio images of 3C236 (e.g., Barthel et al. 1985; Mack et al. 1997) indicate that diffuse radio emission is more pronounced in the west lobe while a significant dominance of double bright hot spots is recognized in the east one. The central region of the west lobe was placed at the nominal position of the X-Ray Telescope (XRT: Serlemitsos et al. 2007) for the XIS. We fixed the satellite roll angle at  $300^\circ$ , in order to avoid contamination on to the west lobe from calibration sources at the specific corners of the XIS field-of-view, and distortion by the anomalous columns of XIS 0.<sup>1</sup> Unfortunately, in this configuration, the

<sup>1</sup> See sub-subsection 7.1.2 of the Suzaku Technical Description ([http://www.astro.isas.jaxa.jp/suzaku/doc/suzaku\\_td/](http://www.astro.isas.jaxa.jp/suzaku/doc/suzaku_td/)).

3C 236 nucleus is located slightly outside the XIS field-of-view. We observed another sky field on the southwest of the west lobe field, which is known to be relatively free from contaminating bright X-ray point sources (e.g., Voges et al. 1999), and evaluated the X-ray background (XRB) spectrum. This XRB field has not yet been observed with ASCA, Chandra, or XMM–Newton.

The present paper deals with the XIS results only, because no significant X-ray signals were detected with the Hard X-ray Detector (Takahashi et al. 2007) from both sky fields. The standard software package, HEASoft 6.16, was adopted for data reduction and analysis. We referred to the calibration database (CALDB) as of 2014 July 1 and 2011 June 30 for the XIS and XRT, respectively. All the XIS events were reprocessed with the Suzaku tool, *aepipeline*. We filtered the data by the following standard criteria; the satellite is outside the South Atlantic Anomaly (SAA), the time after an SAA passage is larger than 436 s, the geomagnetic cut-off rigidity is higher than 6 GV, the source elevation is higher than  $20^\circ$  and  $5^\circ$  above the rim of day and night Earth, respectively, and the XIS data are unaffected by telemetry saturation. The filtering procedures yielded 78.0 and 42.4 ks of good exposures for the west-lobe and XRB fields, respectively.

In the scientific analysis below, we picked up those events with an XIS grade of 0, 2, 3, 4, or 6. In order to mitigate the artificial increase in the non-X-ray background (NXB) level related to the charge injection, those pixels flagged as SCI\_2ND\_TRAILING\_ROW were masked out for the backside-illuminated (BI) CCD chip (XIS 1).<sup>2</sup>

## 2.2 Archival Chandra data

Thanks to its sub-arcsecond angular resolution, Chandra is very useful to evaluate the X-ray flux of possible contaminating faint point-like sources located within the west lobe, which are unresolved with the Suzaku XIS. 3C 236 has been observed by the Chandra ACIS-I array with three exposures. Among them, we selected the observation aiming at its west lobe (ObsID = 10246; see table 1).

The ACIS data were reduced with the software package CIAO 4.6. We reprocessed the data and created a new level 2 event file with the tool *chandra\_repro*, by referring to CALDB 4.6.2. Because the NXB count rate integrated over the whole ACIS-I array was found to be fairly stable throughout the observation, we performed no additional data screening on the new level 2 event file. Correspondingly, we obtained 29.4 ks of good exposure on the west lobe. When the science products were derived, a grade

selection criterion similar to that for the Suzaku XIS (i.e., 0, 2, 3, 4, or 6) was applied.

## 3 Image analysis

The left-hand panel of figure 1 displays the XIS image of the 3C 236 west lobe. Here, we extracted the XIS events in the 0.5–5.5 keV range, where the observed data are free from photons from the calibration sources at the field-of-view corners. The data from all the CCD chips (XIS 0, 1, and 3) were summed up. Neither the XRB nor NXB was subtracted. The image was smoothed with a two-dimensional Gaussian kernel of  $30''$  radius. The radio image of 3C 236 at 608.5 MHz (Mack et al. 1997)<sup>3</sup> was superposed with contours. The left-hand panel of figure 1 suggests faint X-ray emission associated with the west lobe, although it is certainly contaminated by several unresolved X-ray sources behind the lobe.

The Chandra ACIS-I image of the same sky field in 0.5–7 keV is presented in the right-hand panel of figure 1. The image clearly reveals numbers of point-like X-ray sources. We performed a source detection procedure using the CIAO tool *wave\_detect* with a standard parameter set. The exposure and point-spread-function maps over the ACIS field-of-view was correctly taken into account for the source detection. In total, 44 X-ray sources were detected with a significance of  $t > 3\sigma$  within the ACIS field-of-view. These sources are plotted with circles or boxes in figure 1.

Utilizing the 608.5 MHz radio map, we evaluated the size of the west lobe. The standard deviation,  $\sigma_r$ , of the radio intensity in the source-free pixels was regarded as the noise level of the radio map. The emission region was defined as those pixels with a radio surface brightness of  $\geq 3\sigma_r$ . We successfully approximated the envelope of the emission region of the west lobe by an ellipse, which is shown in figure 1 by the solid line. After deconvolving the radio beam size, the ellipse has a major and minor radius of  $6'74$  and  $2'78$ , respectively, corresponding to the projected sizes of 740 and 305 kpc at the redshift of 3C 236. The X-ray spectrum from the west lobe is accumulated in this ellipse (see subsection 4.3). On the region, the 15 Chandra sources, plotted with the circles in figure 1, were detected. These sources are listed in table 2.

## 4 Spectral analysis

### 4.1 X-ray background

It is inevitably required to subtract the NXB and XRB levels precisely, for the spectral analysis of extended X-ray

<sup>2</sup> See “Amount of Charge Injection for XIS 1 and NXB Increase with CI=6 keV” ([http://www.astro.isas.jaxa.jp/suzaku/analysis/xis/xis1\\_ci\\_6\\_nxb/](http://www.astro.isas.jaxa.jp/suzaku/analysis/xis/xis1_ci_6_nxb/)).

<sup>3</sup> The electric version is available from the NASA/IPAC Extragalactic Database (NED), operated by the Jet Propulsion Laboratory, California Institute of Technology, under contract with the National Aeronautics and Space Administration.

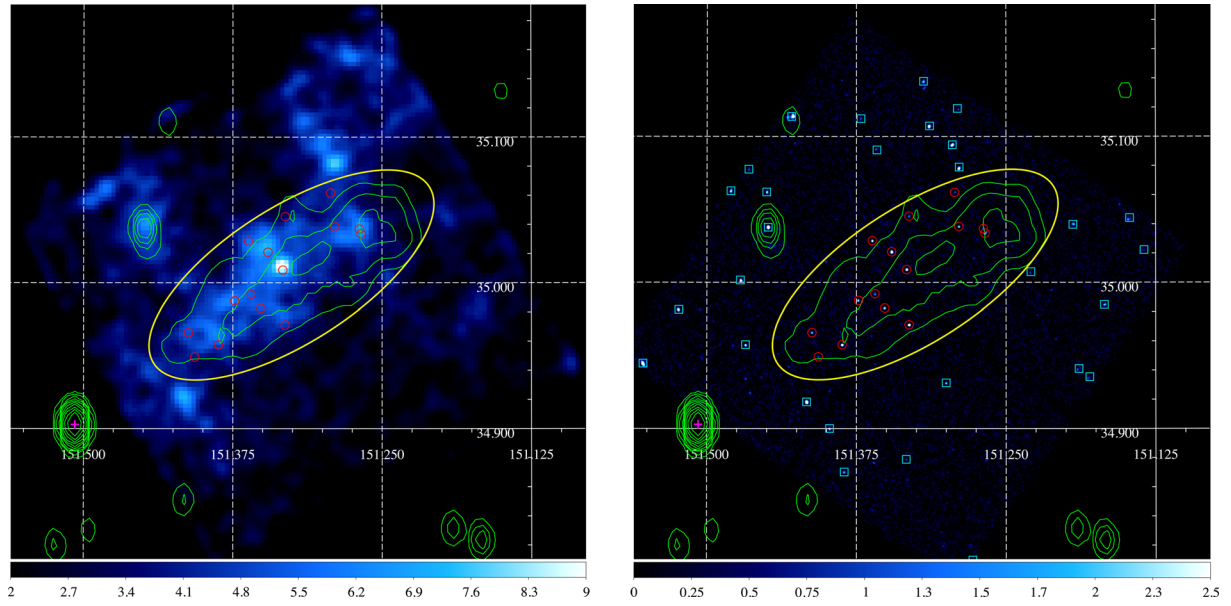


**Fig. 1.** (Left) Background-inclusive Suzaku XIS image of the 3C 236 west lobe in the 0.5–5.5 keV range, on which the 608.5 MHz radio contours (Mack et al. 1997) are superposed. The XIS image was smoothed with a two-dimensional Gaussian kernel of a  $30''$  radius, while it was uncorrected for exposure. The scale bar indicates the signal counts within a  $10'' \times 10''$  bin. The XIS spectrum of the west lobe was accumulated from the solid ellipse. The circles mark the contaminating Chandra ACIS sources, taken into account in the XIS spectral analysis (see tables 2 and 4). The nucleus of 3C 236, shown with the cross, is located outside the XIS field-of-view. (Right) Background-inclusive Chandra ACIS image of the similar sky field in 0.5–7 keV, smoothed with a two-dimensional Gaussian of a  $4''$  radius. The scale bar displays the signal counts within a  $2'' \times 2''$  bin. The X-ray sources detected with the ACIS inside the XIS spectral integration region (the ellipse) are overplotted with the circles, while those outside the region are indicated by the boxes. (Color online)

**Table 2.** Chandra X-ray sources detected inside the ellipse, representing the west lobe.

(RA, Dec)	$\Delta\theta^*$	$t^\dagger$
(151°29288, +35°06163)	1.2	3.2
(151°33095, +35°04535)	0.7	4.5
(151°28930, +35°03829)	0.3	6.4
(151°26875, +35°03690)	0.9	4.3
(151°26740, +35°03364)	0.8	8.0
(151°36171, +35°02858)	0.1	10.7
(151°34551, +35°02092)	0.1	30.7
(151°33296, +35°00870)	0.1	18.9
(151°35938, +34°99214)	0.2	4.9
(151°37328, +34°98764)	0.2	8.6
(151°35123, +34°98246)	0.1	10.1
(151°33097, +34°97106)	0.1	22.4
(151°41207, +34°96578)	0.3	6.1
(151°38690, +34°95742)	0.1	16.4
(151°40676, +34°94915)	0.6	3.6

\*The position error in arcseconds.  $^\dagger$ The detection significance.

emission with a low surface brightness. It is reported that the NXB level of the XIS can be predicted with an accuracy of  $\sim 3\%$  for a typical exposure of 50 ks by utilizing the `xisnxbgen` tool (Tawa et al. 2008). We make use of the XIS data accumulated from the XRB field (see table 1) to model the XRB spectrum in the direction to 3C 236.

The 0.5–5.5 keV XIS image of the XRB field is plotted in figure 2. We extracted the XRB spectrum within the solid rectangle in the image. The region is selected so as not to be affected by the anomalous columns of the XIS 0. In addition to the previously known X-ray sources (the crosses in figure 2), listed in the Second ROSAT Source Catalog of Pointed Observations with the Position Sensitive Proportional Counter,<sup>4</sup> a few point sources and faint extended X-ray emission were recognized within the regions. Then, the dashed rectangle and circles in the image were discarded. Figure 3 shows the XRB spectrum derived from the region, after the NXB spectrum generated by `xisnxbgen` was subtracted. We co-added the data from the two front-illuminated (FI) CCD chips (XIS 0 and 3). The XIS response matrix functions (rmfs) of this region were created by `xisrmfgen`. Assuming a diffuse source with a radius of  $20'$ , which has a flat spatial distribution, we simulated the auxiliary response files (arfs) by `xissimarfgen` (Ishisaki et al. 2007).

The 0.2–10 keV XRB spectrum is widely known to be decomposed into a power-law (PL) component and a two-temperature thermal plasma emission (Kushino et al. 2002; Lumb et al. 2002). The PL component is reported to exhibit an average surface brightness of

<sup>4</sup> Taken from (<http://www.xray.mpe.mpg.de/cgi-bin/rosat/src-browser>).



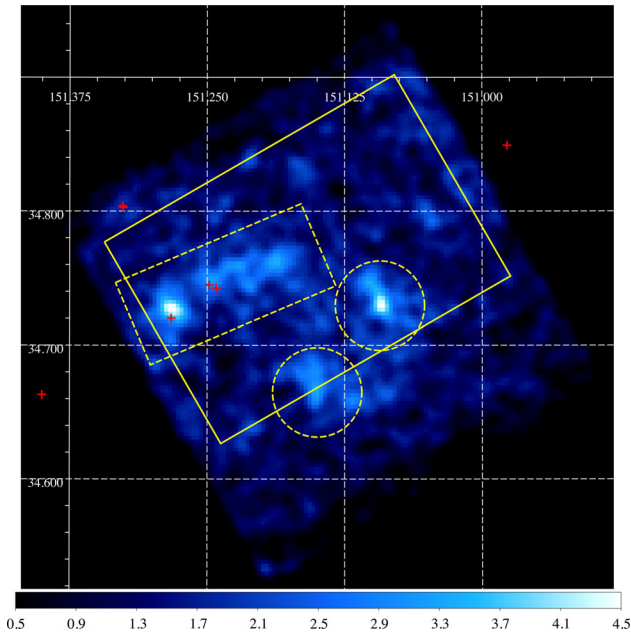


**Fig. 2.** Suzaku XIS image of the XRB region in 0.5–5.5 keV, smoothed with a two-dimensional Gaussian function of a  $30''$  radius. The integration region for the XRB spectrum is indicated by the solid rectangle, from which the dashed rectangle and two circles were removed. The X-ray sources, taken from the Second ROSAT Source Catalog of Pointed Observations with the Position Sensitive Proportional Counter, are indicated by the crosses. (Color online)

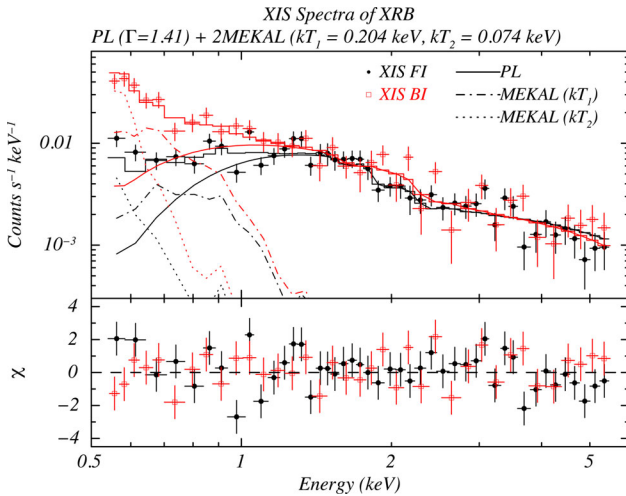


**Fig. 3.** NXB-subtracted Suzaku XIS spectrum of the XRB. The best-fitting model, comprising a PL component ( $\Gamma = 1.41$ ; solid line) and two MEKAL ones ( $kT_1 = 0.204$  keV and  $kT_2 = 0.074$  keV; the dash-dotted and dotted lines, respectively), is indicated by the histograms. (Color online)

$f_{\text{PL}} = (6.4 \pm 0.6) \times 10^{-8} \text{ erg cm}^{-2} \text{ s}^{-1} \text{ str}^{-1}$  in 2–10 keV, with a rather small spatial fluctuation of  $\sim 7\%$ . Its photon index is accurately determined as  $\Gamma = 1.41$  (Kushino et al. 2002). This component is believed to be dominated by unresolved faint sources, including distant active galactic nuclei.

**Table 3.** Best-fitting spectral parameters for the XRB.

Parameter	Value
$N_{\text{H}} (\text{cm}^{-2})$	$9.3 \times 10^{19*}$
$\Gamma$	$1.41^\dagger$
$kT_1$	$0.204^\ddagger$
$kT_2$	$0.074^\ddagger$
$f_{\text{tot}} (\text{erg s}^{-1} \text{ cm}^{-2} \text{ str}^{-1})^\S$	$(6.1 \pm 0.2) \times 10^{-8}$
$f_{\text{PL}} (\text{erg s}^{-1} \text{ cm}^{-2} \text{ str}^{-1})^\parallel$	$4.6 \times 10^{-8}$
$f_{\text{th}} (\text{erg s}^{-1} \text{ cm}^{-2} \text{ str}^{-1})^\#$	$2.5 \times 10^{-8}$
$\chi^2/\text{dof}$	95.8/79

\*Fixed at the Galactic value (Kalberla et al. 2005).  $^\dagger$ Taken from Kushino et al. (2002).  $^\ddagger$ Taken from Lumb et al. (2002).  $^\S$ The total absorption-inclusive surface brightness in 0.5–5 keV.  $^\parallel$ The absorption-inclusive surface brightness of the PL component in 2–10 keV.  $^\#$ The absorption-inclusive surface brightness in 0.5–2 keV, summed over the two MEKAL components.

By adopting the MEKAL code (Mewe et al. 1985), the temperatures of the thermal plasma emission were determined as  $kT_1 = 0.204$  keV and  $kT_2 = 0.074$  keV (Lumb et al. 2002). The thermal components are thought to be of Galactic and local origin, and the surface brightness is reported to be highly variable from field to field.

We fitted the XIS spectrum from the XRB region with a composite model consisting of the PL component ( $\Gamma = 1.41$ ) and the two MEKAL ones ( $kT_1 = 0.204$  keV and  $kT_2 = 0.074$  keV). All the components were subjected to the Galactic absorption toward 3C 236 with a hydrogen column density of  $N_{\text{H}} = 9.3 \times 10^{19} \text{ cm}^{-2}$  (Kalberla et al. 2005). The model was found to be reasonable ( $\chi^2/\text{dof} = 95.8/79$ ), yielding the best-fitting parameters tabulated in table 3. The measured 2–10 keV surface brightness of the PL component,  $f_{\text{PL}} = 4.6 \times 10^{-8} \text{ erg cm}^{-2} \text{ s}^{-1} \text{ str}^{-1}$ , falls near the lowest end of the XRB surface brightness distribution (Kushino et al. 2002). Therefore, we have judged that the best-fitting XRB model is safely applied to the spectral analysis of the west lobe.

## 4.2 Contaminating point sources

The Chandra ACIS signals from each X-ray source, detected in the integration region for the XIS spectrum from the west lobe (the ellipse in figure 1), were integrated within a circle of a 10 pixel ( $4''.9$ ) radius centered on the source position (see table 2). The NXB plus XRB events were accumulated from a concentric annulus with a radius of 15–30 pixel ( $7''.4$ – $14''.8$ ). The spectral files, together with the rmf and arf ones, were created by the CIAO script `specextract`. The energy-dependent aperture correction was applied to the arfs.

Due to low signal statistics for the individual sources, we present the ACIS spectrum summed over the 15 sources in

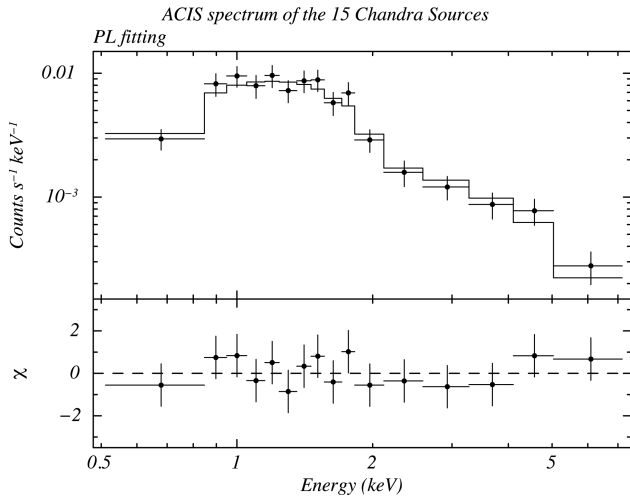


**Fig. 4.** Sum of the Chandra ACIS spectra from the 15 sources detected on the west lobe (table 2). The histogram indicates the best-fitting PL model.

**Table 4.** Best-fitting parameters for the summed spectrum of the 15 contaminating sources on the west lobe.

Parameter	Value
$N_{\text{H}}$ ( $\text{cm}^{-1}$ )	$1.3^{+1.2}_{-1.0} \times 10^{21}$
$\Gamma$	$2.0 \pm 0.3$
$F_{\text{src}}$ ( $\text{erg s}^{-1} \text{cm}^{-2}$ )*	$(1.2 \pm 0.1) \times 10^{-13}$
$\chi^2/\text{dof}$	6.9/13

\*The 0.5–5 keV absorption-inclusive flux.

figure 4. The rmf was simply averaged over these sources, after it was multiplied by the corresponding arf. The spectrum was successfully approximated by a PL model modified by a free absorption ( $\chi^2/\text{dof} = 6.9/13$ ). The best-fitting parameters are summarized in table 4. The summed absorption-inclusive X-ray flux from the sources was measured as  $F_{\text{src}} = (1.2 \pm 0.1) \times 10^{-13} \text{ erg s}^{-1} \text{ cm}^{-2}$  in 0.5–5 keV. The photon index,  $\Gamma = 2.0 \pm 0.3$ , was found to agree with a typical value of nearby active galaxies in a similar energy range (Miyazawa et al. 2009).

### 4.3 West lobe

#### 4.3.1 Significant excess signals

Figure 5 shows the XIS spectra of the west lobe integrated within the ellipse in figure 1, after the NXB events simulated by the `xisnxbgen` tool were subtracted. The data below 0.6 keV were discarded, since we noticed considerable inconsistency between the XIS FI and BI data in the spectral fitting over this energy range, probably due to the calibration uncertainty. The signal statistics from the region in the 0.6–5.0 keV range are summarized in table 5.

We adopted the typical NXB systematic uncertainty of 3% (Tawa et al. 2008). Significant X-ray signals exceeding the NXB were detected, with FI and BI count rates per one CCD chip of  $(1.94 \pm 0.04 \pm 0.015) \times 10^{-2} \text{ counts s}^{-1}$  and  $(2.67 \pm 0.07 \pm 0.03) \times 10^{-2} \text{ counts s}^{-1}$ , respectively. Here, the first and second errors represent the statistical and systematic ones, respectively.

The NXB-subtracted XIS spectra of the west lobe plotted in figure 5 inevitably include the XRB signals and contamination from the point sources, in addition to the signals from the west lobe itself. In the similar manner to that adopted in subsection 4.1, the rmf and arf of the west lobe region to the XRB were generated. The dash-dotted lines in the left-hand panel of figure 5 indicate the XRB model spectrum (table 3), which is convolved with the XIS rmf and arf. The FI and BI count rates of the XRB within the west lobe region in 0.6–5.0 keV were estimated as  $(1.01 \pm 0.03) \times 10^{-2} \text{ counts s}^{-1}$  and  $(1.44 \pm 0.04) \times 10^{-2} \text{ counts s}^{-1}$ , respectively.

The rmfs and arfs of the west lobe region to the 15 Chandra X-ray sources listed in table 2 were individually calculated, and they were simply averaged over all the sources. The best-fitting PL model for the sum of the Chandra spectra from these sources (see figure 4 and table 4) is drawn with the dotted lines in the left-hand panel of figure 5, after it is convolved with the averaged rmf and arf. The contamination from these sources on to the 0.6–5.0 keV FI and BI count rates of the west lobe were estimated as  $(0.58 \pm 0.03) \times 10^{-2} \text{ counts s}^{-1}$  and  $(0.73 \pm 0.04) \times 10^{-2} \text{ counts s}^{-1}$ , respectively. We neglected the Chandra sources detected outside the signal integration region, since their contribution is inferred as at most 9% of the sum signals from the 15 sources.

The solid lines in the left-hand panel of figure 5 present the sum spectrum of the XRB and source contamination. The residuals plotted in the bottom clearly visualize excess signals over these two components ( $\chi^2/\text{dof} = 249.1/134$ ). The 0.6–5.0 keV excess count rate is estimated as  $(0.35 \pm 0.04 \pm 0.05) \times 10^{-2} \text{ counts s}^{-1}$  and  $(0.50 \pm 0.07 \pm 0.07) \times 10^{-2} \text{ counts s}^{-1}$  with the XIS FI and BI, respectively. Here and hereafter, the errors of the best-fitting spectral models for the XRB and for the contaminating sources were propagated to the systematic error (i.e., the second one). Thus, the statistical significance of the excess with the FI and BI was evaluated as  $8.7\sigma$  and  $7.4\sigma$ , respectively. Even if the systematic errors are taken into account, the excess has remained meaningful.

#### 4.3.2 Spectral modeling

In order to reproduce the excess spectrum from the west lobe region, we employed an additional absorbed PL component. The arf to this PL component is calculated for a

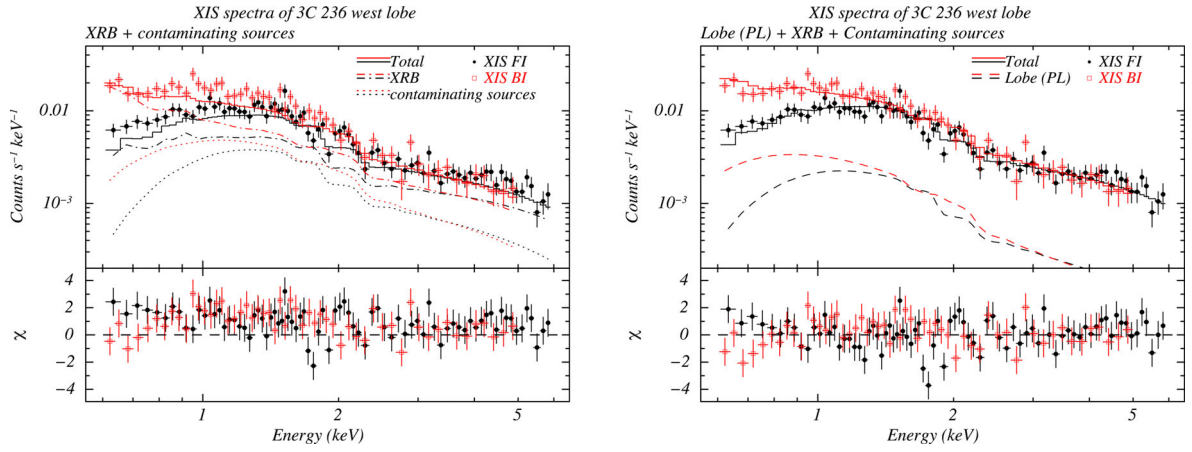


**Fig. 5.** NXB-subtracted XIS spectra of the 3C 236 west lobe. In the left-hand panel, the XIS data are compared with the spectral model (the solid histogram) consisting of the XRB (the dash-dotted lines) and the contamination from the Chandra X-ray sources detected on the west lobe (the dotted lines). The residual spectrum is plotted in the bottom layer. In the right-hand panel, the excess over the XRB plus contamination source model is fitted by an additional PL component (the dashed lines), representing the X-ray emission from the west lobe. (Color online)

**Table 5.** Signal statistics from the west lobe region.

Component	FI signal ( $10^{-2}$ counts $s^{-1}$ )*			BI signal ( $10^{-2}$ counts $s^{-1}$ )*		
	Rate	$\sigma_{\text{stat}}^{\dagger}$	$\sigma_{\text{sys}}^{\ddagger}$	Rate	$\sigma_{\text{stat}}^{\dagger}$	$\sigma_{\text{sys}}^{\ddagger}$
Data	2.44	0.04	—	3.65	0.07	—
NXB	0.50	0.005	0.015	0.98	0.02	0.03
Signal	1.94	0.04	0.015	2.67	0.07	0.03
XRB	1.01	—	0.03	1.44	—	0.04
Sources <sup>§</sup>	0.58	—	0.03	0.73	—	0.04
Excess <sup>#</sup>	0.35	0.04	0.05	0.50	0.07	0.07

\*Count rate per one CCD chip evaluated in 0.6–5 keV. <sup>†</sup>Statistical error. <sup>‡</sup>Systematic error. <sup>§</sup>Contamination from the 15 Chandra sources detected on the west lobe region. <sup>#</sup>Excess signals, after the NXB, XRB and source contamination were subtracted.

diffuse source filling the ellipse in figure 1 with a uniform surface brightness. First, we fitted the XIS spectrum with the photon index  $\Gamma$  and absorption column density  $N_{\text{H}}$  both left free. The confidence map in figure 6 visualizes that the Galactic absorption toward 3C 236 with the column density of  $N_{\text{H}} = 9.3 \times 10^{19} \text{ cm}^{-2}$  (Kalberla et al. 2005) is fairly preferable, although the acceptable range is found to be slightly wide. Morganti, Tadhunter, and Oosterloo (2005) reported a massive nuclear outflow of neutral gas with a column density of  $N_{\text{H}} = 5 \times 10^{21} \text{ cm}^{-2}$ , which could affect the nuclear jet emission. Such a high column density, which requires a very soft spectrum ( $\Gamma \gtrsim 4$ ), is outside the 98% statistical confidence range. We think that the nuclear outflow should not impinge upon the X-ray emission from the Mpc-scale lobe, since it is reported to exhibit a spatial extent of only  $\sim 1$  kpc.

Based on the argument above, we decided to adopt the Galactic absorption for the west lobe. The excess spectrum is successfully described with the PL model modified by

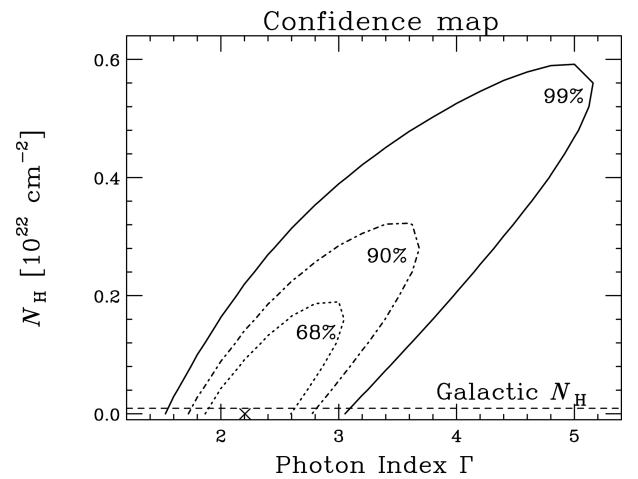


**Fig. 6.** Confidence contours on the  $\Gamma$ – $N_{\text{H}}$  plane for the additional PL component fitted to the excess XIS spectrum of the west lobe. Three confidence levels are indicated at 68%, 90%, and 99%, with the dotted, dash-dotted, and solid lines, respectively. The cross marks the best-fitting values ( $\Gamma = 2.20$  and  $N_{\text{H}} = 3.0 \times 10^{16} \text{ cm}^{-2}$ ). The horizontal dashed line corresponds to the Galactic column density,  $N_{\text{H}} = 9.3 \times 10^{19} \text{ cm}^{-2}$ .

**Table 6.** Summary of the PL fitting to the excess emission from the west lobe.

Parameter	Case 1	Case 2
$N_H$ (cm $^{-2}$ )	$9.3 \times 10^{19*}$	
$\Gamma$	$2.23^{+0.44+0.14}_{-0.38-0.12}^\dagger$	$1.74^\ddagger$
$S_X$ (nJy) $^\S$	$15.3^{+3.0}_{-3.1} \pm 1.8^\dagger$	$12.3 \pm 2.0 \pm 1.9^\ddagger$
$\chi^2/\text{dof}$	142.2/132	146.8/133

\*Fixed at the Galactic value (Kalberla et al. 2005).  $^\dagger$ The first and second errors represent the statistical and systematic ones, respectively.  $^\ddagger$ Fixed at the radio photon index in the 326–2695 MHz range.

$^\S$ Flux density at 1 keV.

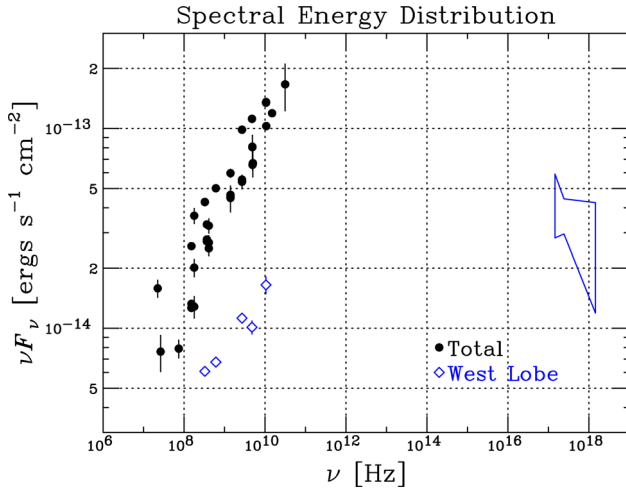


**Fig. 7.** Radio and X-ray spectral energy distribution of 3C 236. The PL model best-fitted to the excess X-ray emission from the west lobe region, corresponding to Case 1 in table 6, is shown with the “bow tie”. Only the statistical errors of  $\Gamma$  and  $S_X$  are taken into account. The synchrotron radio data of the west lobe, estimated by adding the radio flux of the “western lobe” and “western hot spot” in Mack et al. (1997), are plotted with the open diamonds. The filled circles indicate the total radio intensity from 3C 236 (Pilkington et al. 1965; Pauliny-Toth et al. 1966; Kellermann et al. 1969; Adgie et al. 1972; Colla et al. 1973; Kellermann & Pauliny-Toth 1973; Viner & Erickson 1975; Genzel et al. 1976; Witzel et al. 1978; Kühr et al. 1981; Roger et al. 1986; Hales et al. 1988; Becker et al. 1991, 1995; Gregory & Condon 1991; Douglas et al. 1996; Waldram et al. 1996; Mack et al. 1997; Condon et al. 1998; Cohen et al. 2007). (Color online)

Galactic absorption as is indicated by the dashed lines in the right-hand panel of figure 5 ( $\chi^2/\text{dof} = 142.2/132$ ). The best-fitting spectral parameters for the excess are tabulated in table 6 (Case 1). The photon index and flux density at 1 keV are measured as  $\Gamma = 2.23^{+0.44+0.14}_{-0.38-0.12}$  and  $S_X = 15.3^{+3.0}_{-3.1} \pm 1.8$  nJy, respectively.

In figure 7, the spectral energy distribution of the X-ray excess from the west lobe is compared with that of the radio synchrotron emission. The radio data of the west lobe are taken from Mack et al. (1997). Since the X-ray spectral integration region adopted here (the ellipse in figure 1) corresponds to the combination of the *western lobe* and *western hot spot* regions defined in Mack et al. (1997), we evaluated

the radio flux of the west lobe by adding those from these two regions. The low-frequency synchrotron radio photon index of the west lobe was estimated as  $\Gamma_R = 1.74 \pm 0.07$  in the 326–2695 MHz range, where the radio image reveals a dominance of diffuse emission. The best-fitting index of the X-ray excess from the west lobe agrees with this value, within the errors. Therefore, we re-examined the PL model with the photon index fixed at the radio value ( $\Gamma = 1.74$ ). As a result, a reasonable fit ( $\chi^2/\text{dof} = 146.8/133$ ; Case 2 in table 6) was obtained. The flux density of the PL component was derived as  $S_X = 12.3 \pm 2.0 \pm 1.9$  nJy at 1 keV.

## 5 Discussion

### 5.1 Origin of the X-ray emission from the west lobe

After carefully subtracting the NXB, XRB, and source contamination, we have detected the excess X-ray emission associated with the west lobe of the giant radio galaxy 3C 236, with a high significance. Its X-ray spectrum is approximated by the PL model, and the photon index was determined as  $\Gamma = 2.23^{+0.44+0.14}_{-0.38-0.12}$ . This is found to be consistent with the 326–2695 MHz synchrotron radio index  $\Gamma_R = 1.74 \pm 0.07$ , when the statistical and systematic errors are considered. Thus, a reasonable fit was derived, by fixing the photon index at  $\Gamma_R$ . As shown in figure 7, the X-ray spectrum of the west lobe does not smoothly connect to the synchrotron radio one. Therefore, the X-ray emission is not attributable to the highest frequency end of the PL-like synchrotron spectrum from the same electron population as for the radio emission. Referring to the previous X-ray studies on lobes of giant radio galaxies (e.g., Isobe et al. 2009, 2011a, 2011b), these properties are thought to support an IC origin for this X-ray emission.

The synchrotron X-ray hypothesis is further rejected by an argument on the electron radiative time scale. We evaluate the synchrotron lifetime of electrons which could produce the synchrotron X-ray photons, by simply assuming the minimum energy condition (Miley 1980). Because the magnetic field strength under this assumption is found to be not so far from the more realistic value to be discussed in subsection 5.2, the following discussion basically holds. Corresponding to the emission region defined in section 3, the three-dimensional shape of the west lobe is assumed to be an ellipsoid with major and minor radii of 740 and 305 kpc, respectively. From the synchrotron radio flux density,  $S_R = 1.11$  Jy at 608.5 MHz (calculated from Mack et al. 1997), and the spectral slope of  $\Gamma_R = 1.74$ , the minimum energy magnetic field in the west lobe was estimated as  $B_{\text{me}} \sim 0.8 \mu\text{G}$ , neglecting the proton contribution. A similar magnetic field strength was derived by



Schoenmakers et al. (2000) under the equipartition condition as  $B_{\text{eq}} = 0.86 \mu\text{G}$ . In this magnetic field, the synchrotron photons at 1 keV are expected to be radiated from electrons with a Lorentz factor of  $\gamma_e \sim 5 \times 10^8$ . Such electrons are estimated to lose half of their energy on a time scale of  $T_{\text{sync}} = \frac{3m_e c}{4\sigma_T u_{\text{me}}} \gamma_e^{-1} \sim 0.08 \text{ Myr}$  through the synchrotron radiation, where  $m_e$  is the electron mass,  $c$  is the speed of light,  $\sigma_T$  is the Thomson cross-section, and  $u_{\text{me}} = B_{\text{me}}^2/8\pi$  is the minimum-energy magnetic energy density. It is important to note that this  $T_{\text{sync}}$  value overestimates the actual radiative cooling time scale in the lobe of 3C236, since the Compton loss is neglected. Nevertheless, the time scale is shorter than the spectral age of 3C236,  $T_{\text{age}} = 98 \pm 3 \text{ Myr}$  by three orders of magnitude (Schoenmakers et al. 2000). We thus regard the synchrotron X-ray explanation as encountering a serious problem due to the significant radiative loss.

Based on the above consideration, we safely ascribe the detected X-ray emission to the IC radiation from the synchrotron-emitting electrons within the west lobe of 3C236. This result has made 3C236 the largest radio galaxy of which the lobe has ever been studied through the IC photons.

In the case of radio lobes, three candidate seed photon sources for the IC scattering were widely proposed; the synchrotron radio photons in the lobes themselves, the infrared radiation field from the nucleus (Brunetti et al. 1997), and the CMB radiation (Harris & Grindlay 1979). The energy density of the synchrotron radiation spatially averaged over the west lobe is estimated to be very low as  $\gtrsim 10^{-19} \text{ erg cm}^{-3}$  from the radio flux density  $S_R = 1.11 \text{ Jy}$  at 608.5 MHz. The infrared flux density from the nucleus of 3C236, 8.4 mJy at the *K*-band (Skrutskie et al. 2006), is converted to the nuclear monochromatic *K*-band luminosity as  $3 \times 10^{44} \text{ erg s}^{-1}$ . This nuclear photon field yields an infrared energy density of  $4 \times 10^{-16} \text{ erg s}^{-1}$  at the nearest edge of the west lobe, which is located at the projected distance

of  $\sim 450 \text{ kpc}$  from the nucleus. At the redshift of 3C236 ( $z = 0.100500$ ; Hill et al. 1996), the CMB energy density is precisely predicted as  $u_{\text{CMB}} = 6.0 \times 10^{-13} \text{ erg s}^{-1}$ . Therefore, we have concluded that the seed photons are dominantly provided by the CMB radiation and the other candidate sources have only a negligible contribution.

## 5.2 Energetics in the west lobe of 3C236

By comparing the IC X-ray and synchrotron radio spectral energy distributions presented in figure 7, we can measure the energy densities of the electrons and magnetic field,  $u_e$  and  $u_m$ , respectively, in the west lobe of 3C236. The input observables, required to calculate  $u_e$  and  $u_m$ , are listed in the upper columns of table 7. The synchrotron radio flux density and photon index ( $S_R = 1.11 \pm 0.02 \text{ Jy}$  at 608.5 MHz and  $\Gamma_R = 1.74 \pm 0.07$  in the 326–2695 MHz range, respectively) were derived from Mack et al. (1997). We adopted the IC X-ray flux density at 1 keV of  $S_X = 12.3 \pm 2.0 \pm 1.9 \text{ nJy}$  derived in Case 2 where the X-ray photon index was fixed at the radio value. Corresponding to the radio and X-ray spectral slope, the electron number density spectrum was assumed to be a simple PL form described as  $\propto \gamma_e^{-(2\Gamma_R-1)}$ . The volume of the west lobe was estimated as  $V = 8.5 \times 10^{72} \text{ cm}^3$ , since we approximated the shape of the west lobe to be the ellipsoid with the major and minor radius of 740 and 305 kpc, respectively (see section 3 and subsection 5.1).

We analytically evaluated the energetics in the west lobe of 3C236 by referring to Harris and Grindlay (1979). The result is summarized in the lower columns of table 7. Here and hereinafter, the statistical error of  $S_X$  is propagated to the first error, while all the other errors (including those in  $S_R$ ,  $\Gamma_R$ , and so forth) are taken into account in the second one. The specially averaged magnetic field strength is derived as  $B = 0.48_{-0.04-0.10}^{+0.05+0.12} \mu\text{G}$  from the equation (11)

**Table 7.** Summary of energetics in the west lobe of 3C236.

	Parameter	Value	Comments
Input	$S_X$ (nJy)	$12.3 \pm 2.0 \pm 1.9$	Case 2
	$S_R$ (Jy)	$1.11 \pm 0.02$	At 608.5 MHz
	$\Gamma_R$	$1.74 \pm 0.07$	In 326–2695 MHz
	$V$ ( $\text{cm}^3$ )	$8.5 \times 10^{72}$	
Output	$u_e$ ( $10^{-14} \text{ erg cm}^{-3}$ )	$3.9_{-0.7-0.9}^{+0.6+1.0}$	$\gamma_e = 10^3\text{--}10^5$
		$12.6_{-2.1-2.1}^{+2.0+2.3}$	$\gamma_e = 10^2\text{--}10^5$
	$u_m$ ( $10^{-14} \text{ erg cm}^{-3}$ )	$0.92_{-0.15-0.35}^{+0.21+0.52}$	
	$B$ ( $\mu\text{G}$ )	$0.48_{-0.04-0.10}^{+0.05+0.12}$	
	$u_e/u_m$	$4.2_{-1.3-2.3}^{+1.6+4.1}$	$\gamma_e = 10^3\text{--}10^5$
		$13.7_{-4.3-5.7}^{+5.3+8.3}$	$\gamma_e = 10^2\text{--}10^5$

in Harris and Grindlay (1979) described as

$$B^{\alpha_R+1} = \frac{(5.05 \times 10^4)^{\alpha_R} C(\alpha_R) G(\alpha_R) (1+z)^{\alpha_R+3}}{10^{47}} \frac{S_R}{S_X} \left( \frac{\nu_R}{\nu_X} \right)^{\alpha_R}, \quad (1)$$

where  $\alpha_R = \Gamma_R - 1$  is the synchrotron radio index (and hence the IC X-ray) energy index,  $\nu_R$  and  $\nu_X$  are the frequencies at  $S_R$  and  $S_X$ , respectively,  $C(\alpha_R)$  is approximately constant at  $\sim 1.15 \times 10^{31}$  over the range of  $\alpha_R = 0.5-2.0$ , and  $G(\alpha_R)$  is evaluated as  $\simeq 0.5$  at  $\alpha_R = 0.74$  ( $\Gamma_R = 1.74$ ). This magnetic field strength is equivalent to the magnetic energy density of  $u_m = 0.92^{+0.21+0.52}_{-0.15-0.35} \times 10^{-14} \text{ erg cm}^{-3}$ .

For the electron spectral slope of  $(2\Gamma_R - 1) > 2$  (i.e.,  $\Gamma_R > 1.5$ ), the  $u_e$  estimate is known to be rather sensitive to the assumption regarding the minimum Lorentz factor of the electrons. However, it has not yet been observationally explored. Following previous studies (e.g., Isobe et al. 2011b), we first evaluated the energy density of electrons with a Lorentz factor of  $\gamma_e = 10^3-10^5$ , because they are directly observable through the IC and synchrotron radiations. The energy density of these electrons was derived as  $u_e = 3.9^{+0.6+1.0}_{-0.7-0.9} \times 10^{-14} \text{ erg cm}^{-3}$ . This indicates a slight electron-dominant condition in the west lobe, as parameterized by the electron to magnetic field energy density ratio of  $u_e/u_m = 4.2^{+1.6+4.1}_{-1.3-2.3}$ . Secondly, we lowered the minimum electron Lorentz factor down to  $\gamma_e = 10^2$ , since the existence of such low-energy electrons was suggested in a number of strong and compact radio galaxies (Brunetti et al. 1997). In addition, a similar value of the minimum Lorentz factor was adopted to interpret low-frequency radio data of some giant radio galaxies (Orrù et al. 2010). As a result, the electron energy density increased to  $u_e = 12.6^{+2.0+2.3}_{-2.1-2.1} \times 10^{-14} \text{ erg cm}^{-3}$ . Correspondingly, the electron dominance in the lobe was found to become more prominent, as  $u_e/u_m = 13.7^{+5.3+8.3}_{-4.3-5.7}$ .

### 5.3 Overall picture

In figure 8 we plotted the relation between  $u_e$  (for  $\gamma_e = 10^3-10^5$ ) and  $u_m$  in the lobes of radio galaxies, from which the IC X-ray emission was detected (Croston et al. 2005; Konar et al. 2010; Isobe et al. 2011b, and references therein). The figure clearly demonstrates that a typical electron dominance of  $u_e/u_m = 1-100$  is realized in the radio lobes, regardless of their physical size (Isobe et al. 2002, 2005, 2006, 2009, 2011a, 2011b). Our Suzaku result on the west lobe of the giant radio galaxy 3C 236 is found to be fully compatible with this picture.

Due to their low energy densities, the IC-detected giant radio galaxies are distributed in the bottom-left end of the  $u_e-u_m$  plot (i.e., figure 8). In the discussion, we neglect

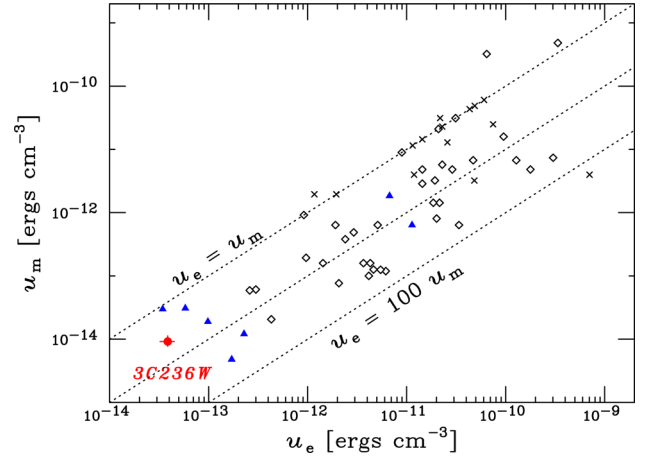


**Fig. 8.** The  $u_e-u_m$  relation in lobes of radio galaxies (Croston et al. 2005; Isobe et al. 2009, 2011a, 2011b; Konar et al. 2010, and reference therein).  $u_e$  is evaluated for the electron Lorentz factor of  $\gamma_e = 10^3-10^5$ . The 3C 236 west lobe is marked by the filled red circle. The lobes of giant radio galaxies ( $D \gtrsim 1$  Mpc) are plotted with the filled blue triangles, while those of moderate radio galaxies are indicated by the open diamonds. For lobes shown by crosses, only the upper limit on the IC X-ray flux (correspondingly the upper and lower limits on  $u_e$  and  $u_m$ , respectively) was determined. The diagonal dotted lines represent the condition of  $u_e/u_m = 1, 10$ , and 100. (Color online)

the lobes of the giant radio galaxy, 3C 457, which is located around the center in figure 8, since it is reported to be one of the youngest sources ( $T_{\text{age}} \sim 30$  Myr: Konar et al. 2010) among the giant radio galaxies. In the lobes of giant radio galaxies, a dominance of the IC radiative loss over the synchrotron one is theoretically pointed out, because their magnetic energy density is predicted to be less than the CMB energy density (Ishwara-Chandra & Saikia 1999). The recent Suzaku results on the giant radio lobes (Isobe et al. 2009, 2011a, 2011b), including our present result on 3C 236, have observationally confirmed this idea, by demonstrating a condition of  $u_m/u_{\text{CMB}} < 0.1$ . In particular, the IC loss is extremely dominant in 3C 236 as  $u_m/u_{\text{CMB}} \sim 0.01$ .

In figure 9, the electron energy density in the lobes are plotted against the total projected length of the radio galaxies,  $D$ . Isobe et al. (2009) proposed that a lobe evolves along a track of  $u_e \propto D^{-2}$  on the plot, while it is actively energized by its jet. The lobe is also predicted to deviate from the  $u_e-D$  track toward a lower  $u_e$  value, due to significant radiative and adiabatic losses, after the energy import by its jet has ceased. The relation of  $u_e \propto D^{-1.9 \pm 0.4}$  observed for the radio galaxies with a moderate size of  $D \lesssim 900$  kpc (the dashed line in figure 9; Isobe et al. 2011b) is thought to qualitatively back up the former idea. The latter scenario was observationally demonstrated by the radio galaxy Fornax A which is reported to host a very dormant nucleus and jet. As is shown in figure 9, the electron energy density in the lobes of Fornax A is more than a factor of 10 smaller

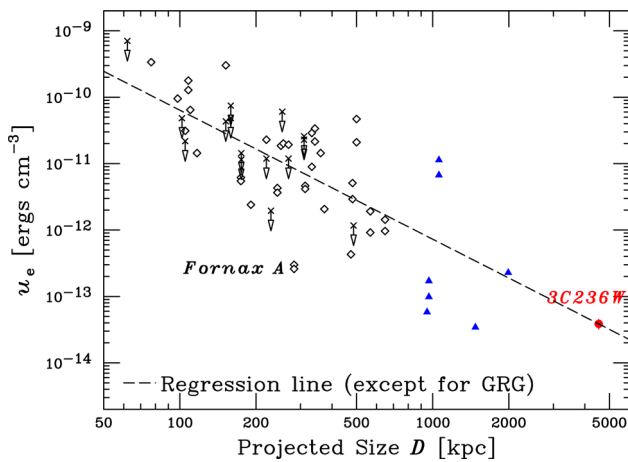


**Fig. 9.** Electron energy density in the lobes,  $u_e$ , plotted as a function of the total projected length,  $D$ , of the radio galaxies. The same symbol/color notation as for figure 8 is adopted. The dashed line indicates the regression line,  $u_e \propto D^{-1.9}$ , for radio galaxies with a moderate size ( $D \lesssim 1$  Mpc). (Color online)

than the value expected from the  $u_e$ – $D$  regression line for the radio galaxies with  $D < 900$  kpc. The recent systematic studies with Suzaku (e.g., Isobe et al. 2011a, 2011b) revealed that the lobes of the giant radio galaxies tend to exhibit a lower  $u_e$  value by nearly an order of magnitude, in comparison to the simple extension of the regression line for the  $D \lesssim 900$  kpc radio galaxies. This is clearly visualized in figure 9. By analogy with Fornax A, this property indicates that the activity of the jets in the giant radio galaxies has already declined, and their energy input to the lobes is currently defeated by the radiative and adiabatic losses of the electrons (Isobe et al. 2011a, 2011b). In contrast,  $u_e$  in the west lobe of 3C236 coincides with the value estimated from the  $u_e$ – $D$  relation for the smaller sources. This result suggests that the lobe is still supplied with sufficient energy from the jet. Even though the current lobe is energetically decoupled from the jet, it has not yet entered a cooling-dominant regime.

The ongoing energy transport (or transport until recently) to the west lobe of 3C236 appears to be reinforced by the observational fact that the radio spectrum around the west hot spot (e.g.,  $\Gamma_R = 1.69$  in 326 MHz–10.6 GHz for the *western hot spot* region in Mack et al. 1998) is harder than those in the surrounding regions. Barthel et al. (1985) closely investigated similarities between the small-scale ( $\sim 2$  kpc) and large-scale ( $\sim$  Mpc) radio structures. They pointed out that the interaction of the jet with the interstellar medium in the central region of 3C236, creating the small-scale structure, continued for more than an order of magnitude longer than  $\sim 10$  Myr. The interaction is inferred to have consequently formed the Mpc-scale lobes. The energy supply to the lobe can be maintained by such a long-lasting interaction.

In contrast, the lack, or weakness, of the radio jet connecting the radio structures in small and large scales especially toward the west direction (Barthel et al. 1985), which is reminiscent of giant double-double radio galaxies (Schoenmakers et al. 1999), implies that the jet activity in 3C236 is highly variable or episodic, rather than stable over its lifetime (e.g., O’Dea et al. 2001; Schilizzi et al. 2001). By comparing the dynamical age of the small-scale structure ( $\gtrsim 0.1$  Myr) and the radiative age of young electrons contained in the hot spots within the large-scale lobes (Mack et al. 1998), O’Dea et al. (2001) proposed that the jet had been possibly switched off for  $\sim 10$  Myr. A high-resolution VLBI image (Schilizzi et al. 2001) supports a recent ignition of a one-sided jet to the west on a 10-mas scale (corresponding to  $\sim 20$  pc at the 3C236 rest frame). The jet reactivation was suggested to be triggered  $\sim 0.1$  Myr ago by a minor merger event that took place  $\sim 10$  Myr ago (Labiano et al. 2013).

We briefly examine the impact of adiabatic and radiative losses during the suggested jet hibernation. When the distance from the nucleus to the lobe edge ( $\sim 1.6$  Mpc) is divided by the source age ( $T_{\text{age}} = 98$  Myr: Schoenmakers et al. 2000), the time-averaged advance speed of the 3C236 west lobe is roughly evaluated as  $\sim 0.05c$ . This agrees with the typical lobe speed measured for Fanaroff–Riley II radio galaxies ( $0.03c$ – $0.1c$ : Alexander & Leahy 1987). At the advance speed, the lobe head proceeds to  $\sim 160$  kpc in 10 Myr. This results in an expansion of the west lobe volume by less than  $\sim 40\%$ . Therefore, the adiabatic loss during the jet dormancy is considered to be relatively insignificant in the 3C236 west lobe. The radiative time scale of the electrons in the west lobe is evaluated as  $\sim 16$  Myr ( $\gamma_e/10^5$ ) $^{-1}$  where both the synchrotron and IC radiation are taken into account. Here, the electron Lorentz factor of  $\gamma_e = 10^5$  corresponds to the synchrotron photons of  $\sim 5$  GHz under the magnetic field strength of  $B = 0.48 \mu\text{G}$  which is measured in this study. This means that the radiative cooling due to the jet hibernation is negligible to the electrons, for which we integrated the energy density  $u_e$  (i.e.,  $\gamma_e = 10^3$ – $10^5$  or  $10^2$ – $10^5$ ). As mentioned above, the flat synchrotron spectrum in the hot spot is compatible with the scenario that the west lobe of 3C236 has not yet been in the cooling domain. Therefore, we have concluded that our result does not contradict the reported suspension of the jet ejection.

Another energy injection channel is hinted in the 1.4 GHz radio image by Barthel et al. (1985), which reveals a wiggling inner ridge in the central region of the west lobe. They interpreted that the ridge was created by a recent jet penetrating the west lobe. This possibly yields a very attractive idea that the new jet re-energizes the west lobe and prevents it from being cooled in the future.

## Acknowledgments

We thank the anonymous reviewer for her/his constructive and supportive suggestions. We are grateful to all the members of the Suzaku team, for the successful operation and calibration. This research has made use of the archival Chandra data and its related software provided by the Chandra X-ray Center (CXC).

## References

- Abdo, A. A., et al. 2010, *Science*, 328, 725
- Adgie, R. L., Crowther, J. H., & Gent, H. 1972, *MNRAS*, 159, 233
- Alexander, P., & Leahy, J. P. 1987, *MNRAS*, 225, 1
- Barthel, P. D., Miley, G. K., Jagers, W. J., Schilizzi, R. T., & Strom, R. G. 1985, *A&A*, 148, 243
- Becker, R. H., White, R. L., & Edwards, A. L. 1991, *ApJS*, 75, 1
- Becker, R. H., White, R. L., & Helfand, D. J. 1995, *ApJ*, 450, 559
- Brunetti, G., Setti, G., & Comastri, A. 1997, *A&A*, 325, 898
- Cohen, A. S., Lane, W. M., Cotton, W. D., Kassim, N. E., Lazio, T. J. W., Perley, R. A., Condon, J. J., & Erickson, W. C. 2007, *AJ*, 134, 1245
- Colla, G., et al. 1973, *A&AS*, 11, 291
- Condon, J. J., Cotton, W. D., Greisen, E. W., Yin, Q. F., Perley, R. A., Taylor, G. B., & Broderick, J. J. 1998, *AJ*, 115, 1693
- Croston, J. H., Hardcastle, M. J., Harris, D. E., Belsole, E., Birkinshaw, M., & Worrall, D. M. 2005, *ApJ*, 626, 733
- Douglas, J. N., Bash, F. N., Bozayan, F. A., Torrence, G. W., & Wolfe, C. 1996, *AJ*, 111, 1945
- Feigelson, E. D., Laurent-Muehleisen, S. A., Kollgaard, R. I., & Fomalont, E. B. 1995, *ApJ*, 449, L149
- Genzel, R., Pauliny-Toth, I. I. K., Preuss, E., & Witzel, A. 1976, *AJ*, 81, 1084
- Gregory, P. C., & Condon, J. J. 1991, *ApJS*, 75, 1011
- Hales, S. E. G., Baldwin, J. E., & Warner, P. J. 1988, *MNRAS*, 234, 919
- Harris, D. E., & Grindlay, J. E. 1979, *MNRAS*, 188, 25
- Hill, G. J., Goodrich, R. W., & Depoy, D. L. 1996, *ApJ*, 462, 163
- Ishisaki, Y., et al. 2007, *PASJ*, 59, S113
- Ishwara-Chandra, C. H., & Saikia, D. J. 1999, *MNRAS*, 309, 100
- Isobe, N., Makishima, K., Tashiro, M., & Hong, S. 2005, *ApJ*, 632, 781
- Isobe, N., Makishima, K., Tashiro, M., Itoh, K., Iyomoto, N., Takahashi, I., & Kaneda, H. 2006, *ApJ*, 645, 256
- Isobe, N., Seta, H., Gandhi, P., & Tashiro, M. S. 2011a, *ApJ*, 727, 82
- Isobe, N., Seta, H., & Tashiro, M. S. 2011b, *PASJ*, 63, S947
- Isobe, N., Tashiro, M., Makishima, K., Iyomoto, N., Suzuki, M., Murakami, M. M., Mori, M., & Abe, K. 2002, *ApJ*, 580, L111
- Isobe, N., Tashiro, M. S., Gandhi, P., Hayato, A., Nagai, H., Hada, K., Seta, H., & Matsuta, K. 2009, *ApJ*, 706, 454
- Kalberla, P. M. W., Burton, W. B., Hartmann, Dap, Arnal, E. M., Bajaja, E., Morras, R., & Poëppel, W. G. L. 2005, *A&A*, 440, 775
- Kaneda, H., et al. 1995, *ApJ*, 453, L13
- Kellermann, K. I., & Pauliny-Toth, I. I. K. 1973, *AJ*, 78, 828
- Kellermann, K. I., Pauliny-Toth, I. I. K., & Williams, P. J. S. 1969, *ApJ*, 157, 1
- Konar, C., Hardcastle, M. J., Croston, J. H., & Saikia, D. J. 2009, *MNRAS*, 400, 480
- Koyama, K., et al. 2007, *PASJ*, 59, S23
- Kühr, H., Witzel, A., Pauliny-Toth, I. I. K., & Nauber, U. 1981, *A&AS*, 45, 367
- Kushino, A., Ishisaki, Y., Morita, U., Yamasaki, N. Y., Ishida, M., Ohashi, T., & Ueda, Y. 2002, *PASJ*, 54, 327
- Labiano, A., et al. 2013, *A&A*, 549, A58
- Laing, R. A., Riley, J. M., & Longair, M. S. 1983, *MNRAS*, 204, 151
- Lumb, D. H., Warwick, R. S., Page, M., & De Luca, A. 2002, *A&A*, 389, 93
- Machalski, J., Koziel-Wierzbowska, D., Jamroz, M., & Saikia, D. J. 2008, *ApJ*, 679, 149
- Mack, K.-H., Klein, U., O'Dea, C. P., & Willis, A. G. 1997, *A&AS*, 123, 423
- Mack, K.-H., Klein, U., O'Dea, C. P., Willis, A. G., & Saripalli, L. 1998, *A&A*, 329, 431
- Mewe, R., Gronenschild, E. H. B. M., & van den Oord, G. H. J. 1985, *A&AS*, 62, 197
- Migliori, G., Grandi, P., Palumbo, G. G. C., Brunetti, G., & Stanghellini, C. 2007, *ApJ*, 668, 203
- Miley, G. 1980, *ARA&A*, 18, 165
- Mitsuda, K., et al. 2007, *PASJ*, 59, S1
- Miyazawa, T., Haba, Y., & Kunieda, H. 2009, *PASJ*, 61, 1331
- Morganti, R., Tadhunter, C. N., & Oosterloo, T. A. 2005, *A&A*, 444, L9
- O'Dea, C. P., Koekemoer, A. M., Baum, S. A., Sparks, W. B., Martel, A. R., Allen, M. G., Macchetto, F. D., & Miley, G. K. 2001, *AJ*, 121, 1915
- Orrù, E., Murgia, M., Feretti, L., Govoni, F., Giovannini, G., Lane, W., Kassim, N., & Paladino, R. 2010, *A&A*, 515, A50
- Pauliny-Toth, I. I. K., Wade, C. M., & Heeschen, D. S. 1966, *ApJS*, 13, 65
- Pilkington, J. D. H., & Scott, J. F. 1965, *MmRAS*, 69, 183
- Roger, R. S., Costain, C. H., & Stewart, D. I. 1986, *A&AS*, 65, 485
- Schilizzi, R. T., et al. 2001, *A&A*, 368, 398
- Schoenmakers, A. P., Mack, K.-H., de Bruyn, A. G., Röttgering, H. J. A., Klein, U., & van der Laan, H. 2000, *A&AS*, 146, 293
- Schoenmakers, A. P., de Bruyn, A. G., Röttgering, H. J. A., & van der Laan, H. 1999, *A&A*, 341, 44
- Serlemitsos, P. J., et al. 2007, *PASJ*, 59, S9
- Skrutskie, M. F., et al. 2006, *AJ*, 131, 1163
- Stawarz, Ł., et al. 2013, *ApJ*, 766, 48
- Strom, R. G., & Willis, A. G. 1980, *A&A*, 85, 36
- Takahashi, T., et al. 2007, *PASJ*, 59, S35
- Takeuchi, Y., et al. 2012, *ApJ*, 749, 66
- Tashiro, M., et al. 1998, *ApJ*, 499, 713
- Tashiro, M. S., Isobe, N., Seta, H., Yaji, Y., & Matsuta, K. 2009, *PASJ*, 61, S327
- Tawa, N., et al. 2008, *PASJ*, 60, S11
- Viner, M. R., & Erickson, W. C. 1975, *AJ*, 80, 931
- Voges, W., et al. 1999, *A&A*, 349, 389
- Waldram, E. M., Yates, J. A., Riley, J. M., & Warner, P. J. 1996, *MNRAS*, 282, 779
- Willis, A. G., Strom, R. G., & Wilson, A. S. 1974, *Nature*, 250, 625
- Witzel, A., Pauliny-Toth, I. I. K., Geldzahler, B. J., & Kellermann, K. I. 1978, *AJ*, 83, 475